

Simulations of Magnetorotational Instability in a Magnetized Couette Flow

Wei Liu

Princeton Plasma Physics Laboratory, Princeton University, P.O. Box 451, Princeton, NJ 08543, USA

wliu@pppl.gov

Jeremy Goodman

Princeton University Observatory, Princeton, NJ 08544, USA

Hantao Ji

Princeton Plasma Physics Laboratory, Princeton University, P.O. Box 451, Princeton, NJ 08543, USA

ABSTRACT

In preparation for an experimental study of magnetorotational instability (MRI) in liquid metal, we present non-ideal two-dimensional magnetohydrodynamic simulations of the nonlinear evolution of MRI in the experimental geometry. The simulations adopt initially uniform vertical magnetic fields, conducting radial boundaries, and periodic vertical boundary conditions. No-slip conditions are imposed at the cylinders. Our linear growth rates compare well with existing local and global linear analyses. The MRI saturates nonlinearly with horizontal magnetic fields comparable to the initial axial field. The rate of angular momentum transport increases modestly but significantly over the initial state. For modest fluid and magnetic Reynolds numbers $Re, Rm \sim 10^2 - 10^3$, the final state is laminar reduced mean shear except near the radial boundaries, and with poloidal circulation scaling as the square root of resistivity, in partial agreement with the analysis of Knobloch and Julien. A sequence of simulations at $Rm = 20$ and $10^2 \lesssim Re \lesssim 10^{4.4}$ enables extrapolation to the experimental regime ($Rm \approx 20$, $Re \sim 10^7$), albeit with unrealistic boundary conditions. MRI should increase the experimentally measured torque substantially over its initial purely hydrodynamic value.

Subject headings: accretion, accretion disk—instability—(magnetohydrodynamics:) MHD —methods: numerical

1. Introduction

Rapid angular momentum transport in accretion disks has been a longstanding astrophysical puzzle. The molecular viscosity of astrophysical gases and plasmas is completely inadequate to explain observationally inferred accretion rates, so that a turbulent viscosity is required. Recent theoretical work (Pringle 1981; Balbus & Hawley 1991; Hawley & Balbus 1991; Balbus & Hawley 1998) indicates that purely hydrodynamic instabilities are absent or ineffective, but that magnetorotational instabilities (MRI) are robust and support vigorous turbulence in electrically-conducting disks. Although originally discovered by Velikhov (1959) and Chandrasekhar (1960), MRI did not come to the attention of the astrophysical community until rediscovered by Balbus & Hawley (1991) and verified numerically (Hawley et al. 1995; Brandenburg et al. 1995; Matsumoto & Tajima 1995). It is now believed that MRI drives accretion in disks ranging from quasars and X-ray binaries to cataclysmic variables and perhaps even protoplanetary disks (Balbus & Hawley 1998). Some astrophysicists, however, argue from laboratory evidence that purely hydrodynamic turbulence may account for observed accretion rates, especially in cool, poorly conducting disks where MRI may not operate (Dubrulle 1993; Richard & Zahn 1999; Duschl et al. 2000; Hure et al. 2001).

Although its existence and importance are now accepted by most astrophysicists, MRI has yet to be clearly demonstrated in the laboratory, notwithstanding the claims of Sisan et al. (2004), whose experiment proceeded from a background state that was not in MHD equilibrium. Recently (Ji et al. 2001; Goodman & Ji 2002), we have therefore proposed an experimental study of MRI using a magnetized Couette flow: that is, a conducting liquid (gallium) bounded by concentric differentially rotating cylinders and subject to an axial magnetic field. The radii of the cylinders are $r_1 < r_2$, as shown in Fig. 1; their angular velocities, Ω_1 & Ω_2 , have the same sign in all cases of interest to us. If the cylinders were infinitely long—very easy to assume theoretically, but rather more difficult to build experimentally—the steady-state solution would be ideal Taylor-Couette flow:

$$\Omega(r) = a + \frac{b}{r^2} \quad (1)$$

where $a = (\Omega_2 r_2^2 - \Omega_1 r_1^2)/(r_2^2 - r_1^2)$ and $b = r_1^2 r_2^2 (\Omega_1 - \Omega_2)/(r_2^2 - r_1^2)$. In the unmagnetized and inviscid limit, such a flow is linearly axisymmetric stable if and only if the specific angular momentum increases outwards: that is, $(\Omega_1 r_1^2)^2 < (\Omega_2 r_2^2)^2$, or equivalently, $ab > 0$. A vertical magnetic field may destabilize the flow, however, provided that the angular *velocity* decreases outward, $\Omega_2^2 < \Omega_1^2$; in ideal MHD, instability occurs at arbitrarily weak field strengths (Balbus & Hawley 1991). The challenge for experiment, however, is that liquid-metal flows are very far from ideal on laboratory scales. While the fluid Reynolds number $Re \equiv \Omega_1 r_1 (r_2 - r_1)/\nu$

can be large, the corresponding *magnetic* Reynolds number

$$Rm \equiv \frac{\Omega_1 r_1 (r_2 - r_1)}{\eta} \quad (2)$$

is modest or small, because the magnetic Prandtl number $P_m \equiv \nu/\eta \sim 10^{-6}$ in liquid metals. Standard MRI modes will not grow unless both the rotation period and the Alfvén crossing time are shorter than the timescale for magnetic diffusion. This requires both $Rm \gtrsim 1$ and $S \gtrsim 1$, where

$$S \equiv \frac{V_A (r_2 - r_1)}{\eta} \quad (3)$$

is the Lundquist number, and $V_A = B/\sqrt{4\pi\rho}$ is the Alfvén speed. Therefore, $Re \gtrsim 10^6$ and fields of several kilogauss must be achieved in typical experimental geometries.

Recently, it has been discovered that MRI modes may grow at much reduced Rm and S in the presence of a helical background field, a current-free combination of axial and toroidal field (Hollerbach & Rüdiger 2005; Rüdiger et. al. 2005). We have investigated these helical MRI modes. While we confirm the quantitative results given by the authors just cited for the onset of instability, we have uncovered other properties of the new modes that cast doubt upon both their experimental realizability and their relevance to astrophysical disks. To limit the length of the present paper, we present results for purely axial background fields only. A paper on helical MRI is in preparation.

One may question the relevance of experimental to astrophysical MRI, especially its nonlinear phases. In accretion disks, differential rotation arises from radial force balance between the gravitational attraction of the accreting body and centrifugal force. Thermal and magnetic energies are small compared to orbital energies, at least if the disk is vertically thin compared to its radius. Consequently, nonlinear saturation of MRI cannot occur by large-scale changes in rotation profile. In experiments, however, differential rotation is imposed by viscous or other weak forces, and the incompressibility of the fluid and its confinement by a container allow radial force balance for arbitrary $\Omega(r)$. Thus, saturation may occur by reduction of differential rotation, which is the source of free energy for the instability. In this respect, MRI experiments and the simulations of this paper may have closer astrophysical counterparts among differentially rotating stars, where rotation is subsonic and boundaries are nearly stress-free (Balbus & Hawley 1994; Menou, Balbus, & Spruit 2005). Both in the laboratory and in astrophysics, however, nonlinear MRI is expected to enhance the radial transport of angular momentum. Quantifying the enhanced transport in a Couette flow is a primary goal of the Princeton MRI experiment and of the present paper.

Another stated goal of the Princeton experiment is to validate astrophysical MHD codes in a laboratory setting. Probably the most widely used astrophysical MHD code is ZEUS

(Stone & Norman 1992a,b), which exists in several variants. The simulations of this paper use ZEUS-2D. Like most other astrophysical MHD codes, ZEUS-2D was designed for compressible, ideal-MHD flow with simple boundary conditions: outflow, inflow, reflecting—but not no-slip. ZEUS would not be the natural choice of a computational fluid-dynamicist interested in Couette flow for its own sake. Nevertheless, after modifying ZEUS-2D to incorporate resistivity, viscosity, and no-slip boundary conditions, we find it to be a robust and flexible tool for the subsonic flows of interest to us. It reproduces the growth rates predicted for incompressible flow (§3), and agrees with hydrodynamic laboratory data (Burin et al. 2005); MHD data are not yet available. Of course, all real flows are actually compressible; in an ideal gas of fixed total volume, density changes generally scale $\sim M^2$ when Mach number $V_{\text{flow}}/V_{\text{sound}} < 1$. Incompressibility is an idealization in the limit $M \rightarrow 0$. We have used an isothermal equation of state in ZEUS with a sound speed chosen so that the maximum of $M \leq 1/4$ and obtain quantitative agreement with incompressible codes at the few-percent level (§2).

Most of the parameters of the simulations in §§3-4 are chosen to match those of the experiment. We adopt the same cylinder radii (Fig. 1). The experimental rotation rates of both cylinders (and of the endcaps) are separately adjustable, as is the axial magnetic field. For these simulations, we adopt fixed values within the achievable range: $\Omega_1 = 4000$ rpm & $\Omega_2 = 533$ rpm, $B_{z0} = 5000$ G. We set the density of the fluid to that of gallium, $\rho = 6 \text{ g cm}^{-3}$.

Our simulations depart from experimental reality in two important respects: Reynolds number and vertical boundary conditions. Computations at $Re \gtrsim 10^6$ are out of reach of any present-day code and computer, at least in three dimensions; $Re \sim 10^6$ might just be achievable in axisymmetry, but higher- Re flows are more likely to be three-dimensional, so that an axisymmetric simulation at such a large Re is of doubtful relevance. (The same objection might be leveled at all of our simulations for $Re \gg 10^3$. Those simulations are nevertheless useful for establishing scaling relations, even if the applicability of the relations to real three-dimensional flows is open to question.) We use an artificially large kinematic viscosity so that $Re = 10^2 - 10^{4.4}$, whereas for the true kinematic viscosity of gallium ($\nu \simeq 3 \times 10^{-3} \text{ cm}^2 \text{ s}^{-1}$), $Re \approx 10^7$ at the dimensions and rotation rates cited above. In defense of this approximation, we point to the fact that extrapolations of Ekman-circulation rates and rotation profiles simulated at $Re < 10^4$ agree well with measurements taken at $Re = 10^6$ both in a prototype experiment (Kageyama et al. 2004), and in the present apparatus (Burin et al. 2005). We *are* able to reproduce the experimental values of the dimensionless parameters based on resistivity: $Rm \sim 20$, $S \sim 4$; we also report simulations at $Rm \sim 10^2 - 10^4$. (The actual diffusivity of gallium is $\eta \simeq 2 \times 10^3 \text{ cm}^2 \text{ s}^{-1}$).

Except for hydrodynamic test simulations carried out to compare with incompressible

results and laboratory data (§2), we adopt vertically periodic boundary conditions for all fluid variables, with a periodicity length $L_z = 2h$, where $h = 27.9$ cm is the actual height of the experimental flow. Such boundary conditions are physically unrealistic, but almost all published linear analyses of MRI in Couette flows have adopted them because they permit a complete separation of variables (Ji et al. 2001; Goodman & Ji 2002; Noguchi et al. 2002; Rüdiger & Shalybkov 2002; Rüdiger et al. 2003); an exception is Rüdiger & Zhang (2001). Thus by adopting periodic vertical boundaries, we are able to test our code against well-established linear growth rates and to explore—apparently for the first time in Couette geometry—the transition from linear growth to nonlinear saturation. The imposition of no-slip conditions at finite endcaps introduces important complications to the basic state, including Ekman circulation and Stewartson layers, which we are currently studying, especially as regards their modification by the axial magnetic field. But the experimental apparatus has been designed to minimize these complications (*e.g.* by the use of independently controlled split endcaps) in order to approximate the idealized Couette flows presented here, whose nonlinear development already presents features of interest. This paper is the first in a series; later papers will address the effects of finite endcaps on magnetized flow, helical MRI instabilities, *etc.*

2. Modifications to ZEUS-2D and Code Tests

ZEUS-2D offers the option of cartesian (x, y) , spherical (R, θ) , or cylindrical (z, r) coordinates. We use (z, r) . Although all quantities are assumed independent of the azimuthal angle φ , the azimuthal components of velocity (v_φ) and magnetic field (B_φ) are represented. We have implemented vertically periodic boundary conditions (period = $2h$) for all variables, and conducting radial boundary conditions for the magnetic field. Impenetrable, no-slip radial boundaries are imposed on the velocities. Viscosity and resistivity have been added to the code. In order to conserve angular momentum precisely, we cast the azimuthal component of the Navier-Stokes equation in conservative form:

$$\frac{\partial L}{\partial t} + \frac{\partial}{\partial z} (V_z L + F_z) + \frac{1}{r} \frac{\partial}{\partial r} (r V_r L + r F_r) = 0, \quad (4)$$

in which $L = r V_\varphi$, and F_r and F_z are the viscous angular-momentum fluxes per unit mass,

$$F_z = -\nu \frac{\partial L}{\partial z}, \quad F_r = -\nu r^2 \frac{\partial}{\partial r} \left(\frac{L}{r^2} \right). \quad (5)$$

In the spirit of ZEUS, the viscous part of eq. (4) is implemented as part of the “source” substep. In accord with the Constrained Transport algorithm (Evans & Hawley 1988), which

preserves $\nabla \cdot \mathbf{B} = 0$, resistivity is implemented by an ohmic term added to the electromotive force, which becomes

$$\mathcal{E} = \mathbf{V} \times \mathbf{B} - \eta \nabla \times \mathbf{B}. \quad (6)$$

2.1. Code Tests (1) - Wendl's Low- Re Solution

At $Re \ll 1$ and $Rm = 0$, poloidal flow is negligible and the toroidal flow is steady. V_φ satisfies

$$\nu(\nabla^2 - \frac{1}{r^2})V_\varphi = 0. \quad (7)$$

Wendl (1999) has given the analytic solution of this equation for no-slip vertical boundaries co-rotating with the outer cylinder. This serves as one benchmark for the viscous part of our code; note that the vertical boundary conditions differ from those used in the simulations of §3-4.

Figure 2 compares results from ZEUS-2D with the analytical result. The maximum relative error is less than 3%. We have also calculated the viscous torque across the mean cylinder ($r = (r_1 + r_2)/2$). Wendl's solution predicts $-1.5004 \times 10^9 \text{ g cm}^2 \text{ s}^{-2}$, and our simulations yield $-1.5028 \times 10^9 \text{ g cm}^2 \text{ s}^{-2}$.

2.2. Code Tests (2) - Magnetic Diffusion

If the fluid is constrained to be at rest, then the toroidal induction equation becomes

$$\frac{\partial B_\varphi}{\partial t} = \eta \left(\frac{\partial^2 B_\varphi}{\partial r^2} + \frac{1}{r} \frac{\partial B_\varphi}{\partial r} - \frac{B_\varphi}{r^2} + \frac{\partial^2 B_\varphi}{\partial z^2} \right) \quad (8)$$

An exact solution compatible with our boundary conditions is:

$$\mathbf{B} = \hat{\mathbf{e}}_z B_z^0 + \hat{\mathbf{e}}_\varphi \frac{B_\varphi^0}{r} \cos(kz) \exp(-\eta k^2 t) \quad (9)$$

where k is the wave number, and B_z^0 and B_r^0 are constants.

A comparison of the theoretical and simulated results shows that the error scales quadratically with cell size, as expected for our second-order difference scheme (Table 1).

2.3. Comparison with an Incompressible Code

ZEUS-2D is a compressible code. However our experimental fluid, gallium, is nearly incompressible at flow speeds of interest, which are much less than its sound speed, 2.7 km s^{-1} . As mentioned in §1, we can approximate incompressible flow by using a subsonic Mach number, $M < 1$. However, since ZEUS is explicit, $M \ll 1$ requires a very small time step to satisfy the CFL stability criterion. As a compromise, we have used $M = 1/4$ (based on the inner cylinder) throughout all the simulations presented in this paper. We assume an isothermal equation of state to avoid increases in M by viscous and resistive heating; the nonlinear compressibility and thermodynamic properties of the actual liquid are in any case very different from those of ideal gases, for which ZEUS was written. Figure 3 compares results obtained from ZEUS-2D with simulations performed by Kageyama et al. (2004) using their incompressible Navier-Stokes code.

3. Linear MRI Simulations

In the linear regime, MRI has been extensively studied both locally and globally (Ji et al. 2001; Goodman & Ji 2002; Rüdiger & Zhang 2001; Noguchi et al. 2002; Rüdiger & Shalybkov 2002; Rüdiger et al. 2003). We have used these linear results to benchmark our code.

In the linear analyses cited above, the system is assumed to be vertically periodic with periodicity length $2h$, twice the height of the cylinders. In cylindrical coordinates, the equilibrium states are $\mathbf{B}_0 = B_0 \hat{\mathbf{e}}_z$ and $\mathbf{V}_0 = r\Omega \hat{\mathbf{e}}_\phi$. WKB methods describe the stability of this system very well even on the largest scales (Ji et al. 2001; Goodman & Ji 2002). Linear modes are proportional to $\exp(\gamma t - ik_z z)f(k_r r)$, where γ is the growth rate, and $f(x)$ is an approximately sinusoidal radial function, at least outside boundary layers, whose zeros are spaced by $\Delta x \approx \pi$. The wavenumbers $k_z = n\pi/h$ and $k_r \approx m\pi/(r_2 - r_1)$, where n and m are positive integers. We will consider only the lowest value of k_r ($m = 1$) but allow $n \geq 1$. The initial perturbation is set to an approximate eigenmode appropriate for conducting boundary conditions:

$$\begin{aligned} \delta B_z &= A \sin k_z z \frac{r_1 + r_2 - 2r}{r} & \delta B_r &= k_z A \cos k_z z \frac{(r_2 - r)(r - r_1)}{r} & \delta B_\phi &= 0 \\ \delta V_z &= B \cos k_z z \frac{r_1 + r_2 - 2r}{r} & \delta V_r &= k_z B \sin k_z z \frac{(r_2 - r)(r - r_1)}{r} & \delta V_\phi &= 0. \end{aligned} \quad (10)$$

Evidently, the fast-growing mode dominates the simulations no matter which n is used initially. Figure 4 compares the MRI growth rate obtained from the simulations with those

predicted by global linear analysis (Goodman & Ji 2002) as a function of magnetic Reynolds number.

The radially global, vertically periodic linear analysis of Goodman & Ji (2002) found that the linear eigenmodes have boundary layers that are sensitive to the dissipation coefficients, but that the growth rates agree reasonably well with WKB estimates except near marginal stability. A comparison of the growth rates found by this analysis with those obtained from our simulations is given in Table 2. In the context of the simulations, “ $Re = \infty$ ” means that the explicit viscosity parameter of the code was set to zero, but this does not guarantee inviscid behavior since there is generally some diffusion of angular momentum caused by finite grid resolution. Nevertheless, since the magnetic Reynolds number of the experiment will be about 20 and since $Re/Rm \sim 10^6$, these entries of the table probably most closely approximate the degree of dissipation in the gallium experiment. In Table 2, the largest growth rate predicted by the linear analysis has been marked with an asterisk (*). The simulations naturally tend to be dominated by the fastest numerical mode—that is, the fastest eigenmode of the finite-difference equations, which need not map smoothly into the continuum limit. Fortunately, as asserted by the Table, the fastest growth occurs at the same vertical harmonic n in the simulations as in the linear analysis.

4. Nonlinear Saturation

As noted in §1, instabilities cannot easily modify the differential rotation of accretion disks because internal and magnetic energies are small compared to gravitational ones, and MRI is believed to saturate by turbulent reconnection (Fleming et al. 2000; Sano & Inutsuka 2001). In Couette flow, however, the energetics do not preclude large changes in the rotation profile. As shown by Fig. 5), the differential rotation of the final state is reduced somewhat compared to the initial state in the interior of the flow, and steepened near the inner cylinder.

4.1. Structure of the final state

For moderate dissipation ($Re, Rm \lesssim 10^3$), the final state is steady. Typical flow and field patterns are shown in Figure 6. The poloidal flux and stream functions are defined so that

$$\mathbf{V}_P \equiv V_r \mathbf{e}_r + V_z \mathbf{e}_z = r^{-1} \mathbf{e}_\varphi \times \nabla \Phi, \quad \mathbf{B}_P \equiv B_r \mathbf{e}_r + B_z \mathbf{e}_z = r^{-1} \mathbf{e}_\varphi \times \nabla \Psi, \quad (11)$$

which imply $\nabla \cdot \mathbf{V}_P = 0$ and $\nabla \cdot \mathbf{B}_P = 0$. [Our velocity field is slightly compressible, so that eq. (11) does not quite capture the full velocity field. Nevertheless, the error is small,

and Φ is well defined by $\nabla^2(\Phi \mathbf{e}_\varphi/r) = \nabla \times \mathbf{V}_P$ with periodic boundary conditions in z and $\partial\Phi/\partial z = 0$ on the cylinders.]

The most striking feature is the outflowing “jet” centered near $z = 0$ in Figure 6. The contrast in flow speed between the jet and its surroundings is shown more clearly in Figure 7. Figure 6 also shows that the horizontal magnetic field changes rapidly across the jet, which therefore approximates a current sheet.

The radial flow speed in the jet scales with Rm as (Fig. 8),

$$V_{\text{jet}} \propto Rm^{-0.53}. \quad (12)$$

We find that the radial speed outside the jet scales similarly,

$$V_{\text{external}} \propto Rm^{-0.56} \propto \eta^{0.56}. \quad (13)$$

Mass conservation demands that $V_{\text{jet}} W_{\text{jet}} = V_{\text{external}}(2h - W_{\text{jet}})$, where W_{jet} is the effective width of the jet. Thus we can conclude that this width is independent of magnetic Reynolds number:

$$W_{\text{jet}} \propto Rm^0 \quad (14)$$

Additional support for this conclusion comes from the nearly equal scaling of V_r and Φ with Rm (Fig. 8), which indicates that the spatial scales in the velocity field are asymptotically independent of Rm . The toroidal flow perturbation and toroidal field are comparable to the rotation speed and initial background field, respectively:

$$1.18 \lesssim \max \frac{B_\varphi}{B_{z0}} \lesssim 1.52, \quad 0.28 \lesssim \max \frac{\delta V_\varphi}{r_1 \Omega_1} \lesssim 0.56 \quad (15)$$

We emphasize that the scalings (12)-(15) have been established for a limited range of flow parameters, $10^2 \lesssim Re, Rm \lesssim 10^{4.4}$. The jet is less well defined at lower Rm , especially in the magnetic field. Extrapolation of these scalings to laboratory Reynolds numbers ($Re \gtrsim 10^6$) is risky, and indeed our simulations suggest that the final states are unsteady at high Re and/or high Rm (Fig. 11).

4.2. Angular Momentum Transport

Figure 9 displays the radial profiles of the advective, viscous, and magnetic torques integrated over cylinders coaxial with the boundaries:

$$\Gamma_{\text{advective}}(r) = \int_{-h}^h dz \, \rho r^2 v_r v_\varphi \quad (16)$$

$$\Gamma_{\text{magnetic}}(r) = \int_{-h}^h dz \left(-\frac{r^2 B_r B_\varphi}{4\pi} \right) \quad (17)$$

$$\Gamma_{\text{viscous}}(r) = \int_{-h}^h dz \left[-r^3 \rho \nu \frac{\partial}{\partial r} \left(\frac{v_\varphi}{r} \right) \right] \quad (18)$$

$$\Gamma_{\text{total}}(r) = \Gamma_{\text{advective}}(r) + \Gamma_{\text{magnetic}}(r) + \Gamma_{\text{viscous}}(r) \quad (19)$$

The advective and magnetic torques vanish at r_1 and r_2 because of the boundary conditions but are important at intermediate radii. All components of the torque are positive except near r_2 . The total torque is constant with radius, as required in steady state, but increases from the initial to the final state (Figure 9). From Figure 10, we infer the scalings

$$\frac{\Gamma_{\text{final}} - \Gamma_{\text{initial}}}{\Gamma_{\text{initial}}} \propto Re^{0.5} Rm^0, \quad (20)$$

at least at $Re, Rm \gtrsim 10^3$. In fact, a better fit to the exponent of Re for $Rm = 20$ and $Re \gtrsim 10^3$ would be 0.68 rather than 0.5, but the exponent seems to decrease at the largest Re , and it is ≈ 0.5 for $Rm = 400$, so we take the latter to be the correct asymptotic value.

Representative runs are listed in Table 3. Additional runs have been carried out on coarser grids (smaller N_r, N_z) to check that the values quoted for the torques are independent of spatial resolution to at least two significant figures in the laminar cases ($Re, Rm \lesssim 10^3$) and to better than 10% in the unsteady cases where precise averages are difficult to obtain. In the latter cases, the quoted values in the last two columns have been averaged over radius but not over time.

4.3. Interpretation of the final state

The division of the flow into a narrow outflowing jet and a slower reflux resembles that found by Kageyama et al. (2004) in their hydrodynamic simulations [Fig. 3]. In that case, the jet bordered two Ekman cells driven by the top and bottom endcaps. In the present case, however, Ekman circulation is not expected since the vertical boundaries are periodic, and we must look elsewhere for an explanation of the final state.

Knobloch & Julien (2005, hereafter KJ) have proposed that axisymmetric MRI may saturate in a laminar flow whose properties depend upon the dissipation coefficients ν & η , with a large change in the mean rotation profile, $\Omega(r)$. Although this mechanism of saturation probably cannot apply to thin disks for the reasons given in §1, it is consistent with some aspects of the final state of our Couette-flow simulations: in particular, the scalings (12)-(13)

of the poloidal velocities with Rm ; and the mean rotation profile does indeed undergo a large reduction in its mean shear, except near the boundaries (Fig. 5).

One prominent difference between the final states envisaged by KJ and those found here is the axial lengthscale. KJ assumed the final state to have the same periodicity as the fastest-growing linear MRI mode, although they acknowledged that their theory does not require this. In our case, the linear and nonlinear lengthscales differ: whereas the fastest linear mode has three wavelengths over the length of the simulation (Table 2), the nonlinear state adopts the longest available periodicity length, namely that which is imposed by the vertical boundary conditions. Within that length, the flow is divided between the narrow jet and broad reflux regions. As discussed below, a third and even narrower reconnection region, whose width scales differently in Rm from that of the jet itself, exists within the jet. Another possibly important difference concerns the role of radial boundaries. KJ simply ignored these, yet our jet clearly originates at the inner cylinder (Fig. 6). KJ’s theory predicts that the poloidal flow should be proportional to $Re^{-1/2}$ as well as $Rm^{-1/2}$. Yet, we find that $V_{r,\text{jet}}$ actually *increases* with Re , roughly as $Re^{+1/2}$, up to $Re \sim 10^3$, above which it begins to decline and the flow becomes unsteady.

The jet is probably the part of the flow that corresponds most closely to the “fingers” envisaged by KJ. Let us at least try to understand how the quantities in our jet scale with increasing Rm at fixed Re , even though it is more relevant to the experiment to increase Re at fixed and modest Rm (for the latter, see below).

In steady state, the toroidal component of the electric field vanishes, $E_\varphi = 0$, because the flux through any circuit around the axis is constant. Consequently,

$$[\Phi, \Psi] \equiv \frac{\partial \Phi}{\partial r} \frac{\partial \Psi}{\partial z} - \frac{\partial \Phi}{\partial z} \frac{\partial \Psi}{\partial r} = \eta r \left(\frac{\partial^2}{\partial z^2} + \frac{\partial^2}{\partial r^2} - \frac{1}{r} \frac{\partial}{\partial r} \right) \Psi \equiv \eta r \Delta_* \Psi, \quad (21)$$

The evidence from our simulations is that the peak values of Φ and Ψ scale as $\eta^{1/2}$ and η^0 , respectively, in the nonrestive limit $\eta \rightarrow 0$, $Rm \rightarrow \infty$. The radial velocity $V_r = r^{-1} \partial \Phi / \partial z$ also scales as $\eta^{1/2}$. In order that the two sides of eq. (21) balance, at least one of the derivatives of Ψ must become singular in the limit $\eta \rightarrow 0$. This appears to be the case. In fact, a comparison of the flux contours in Figures 6(a) and 12(a) suggests that a current sheet develops at the center of the jet. This is more obvious in the horizontal components of current density, J_r and J_φ , whose peak values we find to scale as $\propto \eta^{-0.46} \approx Rm^{1/2}$ (Figure 13) and the maximum toroidal magnetic field near the current sheet scales as

$$B_\varphi \propto Rm^{0.18} \approx Rm^{1/6} \quad (22)$$

From these scalings one infers that the width of the current sheet scales as $\eta^{1/3}$. On the

other hand, the region defined by $|B_r|, |B_\phi| > |B_z|$ appears to have a width $\propto \eta^0$, like that of the velocity jet. We call this the magnetic “finger” because of its form in Fig. 12.

It is interesting to check whether these scalings are consistent with the observation that the total torque (radial angular-momentum flux) appears to be asymptotically independent of the resistivity. As $\eta \rightarrow 0$, the advective torque $\propto \int V_r V_\phi dz$ tends to zero since $V_r \propto \eta^{1/2}$ and V_ϕ is presumably bounded by $\sim r\Omega_1$. The viscous contribution is always dominant near the cylinders but is reduced compared to the initial state at intermediate radii by the reduction in the vertically-averaged radial shear (Fig. 9). Since the total torque is larger in the final than in the initial state, a significant fraction of it must be magnetic, and this fraction should be approximately independent of η at sufficiently small η . If $B_r \sim B_\phi \propto \eta^x$ within a vertical layer of width $\Delta z \sim \eta^y$, the torque $\propto \int B_r B_\phi dz \propto \eta^{2x+y}$. Thus we expect $y \approx -2x$. In agreement with this, we have found that $x \approx -1/2$ and $y \approx 1/3$ in the current sheet, while in the finger, $x \approx y \approx 0$.

One notices in Fig. 12(a)&(d) that the angular velocity is approximately constant along field lines— $\Omega = \Omega(\Psi)$ —as required by Ferraro’s Law when the flow is predominantly toroidal and the resistivity small. There must therefore be an outward centrifugal force along the lines in the magnetic finger, which in combination with the reconnection layer, presumably drives the residual radial outflow. Viscosity continues to be essential even as $\eta \rightarrow 0$ because it is then the only mechanism for communicating angular momentum between field lines, and between the fluid and the cylinders; the distortion of the field enhances viscous transport by bringing into closer proximity lines with different angular velocity.

To summarize, in the highly conducting limit $Rm \rightarrow \infty$, $Re = \text{constant}$, there appear to be at least three main regions of the flow: (I) an “external” or “reflux” region in which the magnetic field is predominantly axial and the velocity predominantly toroidal, but with a small ($\propto \eta^{1/2}$) radial inflow; (II) a “jet” or “finger” of smaller but constant vertical width in which the fields are mainly horizontal and there is a more rapid but still $O(\eta^{1/2})$ flow along field lines; (III) a resistive layer or current sheet at the center of the jet whose width decreases as $\eta^{1/3}$, across which the horizontal fields change sign.

4.4. Simulations at small magnetic Prandtl number

In the ongoing Princeton MRI experiment, the experiment material, liquid gallium, has kinematic viscosity $\nu \approx 3 \times 10^{-3} \text{ cm}^2 \text{ s}^{-1}$ and resistivity $\eta \approx 2 \times 10^3 \text{ cm}^2 \text{ s}^{-1}$. The typical dimensionless parameters are $Rm \approx 20$ and $Re \approx 10^7$ at the dimensions and rotation speeds cited above. The magnetic Prandtl number $Pr \equiv Rm/Re \approx 10^{-6}$ is very small. Reliable

simulations with Reynolds number as high as 10^7 are beyond any present-day computer, and small Pr presents additional challenges for some codes.

Although our boundary conditions are not those of the experiment, we have carried out simulations at $Rm = 20$ and much higher Re in order to explore the changes in the flow due to these parameters alone. A simulation for $Re = 25600$ is shown in Figures 14 & 15. All though this is still considerably more viscous than the experimental flow, it is clearly unsteady, like all of our simulations at $Re \gtrsim 3000$. A narrow jet can still be observed in the poloidal velocities, but the poloidal field is only weakly perturbed at this low Rm : $B_{\varphi, \max} \approx 0.1 B_z$.

Since the Reynolds number of the experiment is much larger than that of our simulations, we can estimate the experimental torques only by extrapolation. Extrapolating according to eq. (20) from the highest- Re simulation in Table 3, one would estimate $\Delta\Gamma/\Gamma_{\text{initial}} \sim 35$ at $Re \sim 10^7$. There are, however, reasons for caution in accepting this estimate. On the one hand, the experimental flow may be three-dimensional and turbulent, which might result in an even higher torque in the final state. On the other hand, the viscous torque in the initial state is likely to be higher than in these simulations because of residual Ekman circulation driven by the split endcaps. Nevertheless, we expect an easily measurable torque increase in the MRI-unstable regime.

5. Conclusions

In this paper, we have simulated the linear and nonlinear development of magnetorotational instability in a nonideal magnetohydrodynamic Taylor-Couette flow. The geometry mimics an experiment in preparation except in the vertical boundary conditions, which in these simulations are periodic in the vertical (axial) direction and perfectly conducting at the cylinders; these simplifications allow direct contact with previous linear studies. We have also restricted our study to smaller fluid Reynolds number (Re), and extended it to larger magnetic Reynolds number (Rm), than in the experiment. We find that the time-explicit compressible MHD code ZEUS-2D, which is widely used by astrophysicists for supersonic ideal flows with free boundaries, can be adapted and applied successfully to Couette systems. MRI grows from small amplitudes at rates in good agreement with linear analyses under the same boundary conditions. Concerning the nonlinear final state that results from saturation of MRI, we draw the following conclusions:

- Differential rotation is reduced except near boundaries, as predicted by Knobloch & Julien (2005).

- A steady poloidal circulation consisting of a narrow outflow (jet) and broad inflow is established. The width of the jet is almost independent of resistivity, but it does decrease with increasing Re . The radial speed of the jet $\propto Rm^{-1/2}$.
- There is a reconnection layer within the jet whose width appears to decrease $\propto Rm^{-1/3}$.
- The vertically integrated radial angular momentum flux depends upon viscosity but hardly upon resistivity, at least at higher Rm [eq. (20)].
- The final state is steady and laminar at $Re, Rm \lesssim 10^3$ but unsteady at larger values of either parameter (Figs. 11 & 15.)
- the final state contains horizontal fields comparable to the initial axial field for $Rm \gtrsim 400$, and about a tenth as large for experimentally more realistic values, $Rm \approx 20$.

We emphasize that these conclusions are based on axisymmetric simulations restricted to $10^2 \lesssim Re, Rm \lesssim 10^{4.4}$, and that the boundary conditions are not realistic. This paper is intended as a preliminary exploration of MRI in the idealized Taylor-Couette geometry that has dominated previous linear analyses. We have not attempted to model many of the complexities of a realistic flow. In future papers, we will study vertical boundary conditions closer to those of the planned experiment; work in progress indicates that these may significantly modify the flow.

The authors would like to thank James Stone for the advice on the ZEUS code. This work was supported by the US Department of Energy, NASA under grant ATP03-0084-0106 and APRA04-0000-0152 and also by the National Science Foundation under grant AST-0205903.

REFERENCES

- Balbus, S. & Hawley, J. 1991, ApJ, 376, 214
- . 1994, MNRAS, 266, 769
- . 1998, Rev. Mod. Phys., 70, 1
- Brandenburg, A., Nordlund, A., Stein, R., & Torkelson, U. 1995, ApJ, 446, 741
- Burin, M., Raftopolous, S., Ji, H., Schartman, E., Morris, L., & Cutler, R. 2005, submitted to Experiments in Fluids

- Chandrasekhar, S. 1960, Proc. Nat. Acad. Sci., 46, 253
- Dubrulle, B. 1993, Icarus, 106, 59
- Duschl, W. J., Strittmatter, P. A., & Biermann, P. L. 2000, A&A, 357, 1123
- Evans, C. & Hawley, J. F. 1988, ApJ., 33, 659
- Fleming, T. P., Stone, J. M., & Hawley, J. F. 2000, ApJ, 457, 355
- Goodman, J. & Ji, H. 2002, J. Fluid Mech., 462, 365
- Hawley, J., Gammie, C., & Balbus, S. 1995, ApJ, 470, 742
- Hawley, J. F. & Balbus, S. A. 1991, ApJ, 376, 223
- Hollerbach, R. & Fournier, A. 2004, In: R. Rosner, G. Rüdiger and A. Bonanno (Editors), *MHD Couette Flows: Experiments and Models*, American Inst. of Physics Conf. Proc., 733, 114
- Hollerbach, R. & Rüdiger, G. 2005, Phys. Rev. Lett., 95(12), 124501
- Hure, J. M., Richard, D., & Zahn, J. P. 2001, A&A, 367, 1087
- Ji, H., Goodman, J., & Kageyama, A. 2001, Mon. Not. R. Astron. Soc., 325, L1
- Kageyama, A., Ji, H., Goodman, J., Chen, F., & Shoshan, E. 2004, J. Phys. Soc. Japan., 73, 2424
- Knobloch, E. & Julien, K. 2005, Physics of Fluids, 17, 094106
- Matsumoto, R. & Tajima, T. 1995, ApJ, 445, 767
- Menou, K., Balbus, S. A., & Spruit, H. C. 2005, ApJ, 607, 564
- Noguchi, K., Pariev, V. I., Colgate, S. A., Beckley, H. F., & Nordhaus, J. 2002, ApJ, 575, 1151
- Pringle, J. E. 1981, ARA&A, 19, 137
- Richard, D. & Zahn, J. P. 1999, A&A, 347, 734
- Rüdiger, G., Hollerbach, R., Schultz, M., & Shalybkov, D. A. 2005, Astronomische Nachrichten, 326, 409
- Rüdiger, G. & Shalybkov, D. 2002, Phys. Rev. E., 66, 016307

- Rüdiger, G., Schultz, M., & Shalybkov, D. 2003, *Phys. Rev. E.*, 67, 046312
- Rüdiger, G. & Zhang, Y. 2001, *A&A*, 378, 302
- Sano, T. & Inutsuka, S. 2001, *ApJ*, 561, L179
- Sisan, D. R., Mujica, N., Tillotson, W. A., Huang, Y., Dorland, W., Hassam, A. B., Anton-
sen, T. M., & Lathrop, D. P. 2004, *Phys. Rev. Lett.*, 93, 114502
- Stone, J. & Norman, M. 1992a, *ApJS.*, 80, 753
- . 1992b, *ApJS.*, 80, 791
- Velikhov, E. P. 1959, *J. Expl Theoret. Phys. (USSR).*, 36, 1398
- Wendl, M. C. 1999, *Phys. Rev. E.*, 60, 6192

Fig. 1.— Geometry of Taylor-Couette flow. In the Princeton MRI experiment, $r_1 = 7.1$ cm, $r_2 = 20.3$ cm, $h = 27.9$ cm.

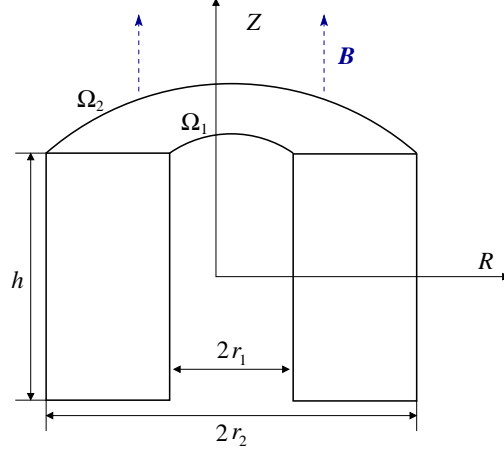


Fig. 2.— Radial profile of the azimuthal velocity for $Re = 1$.

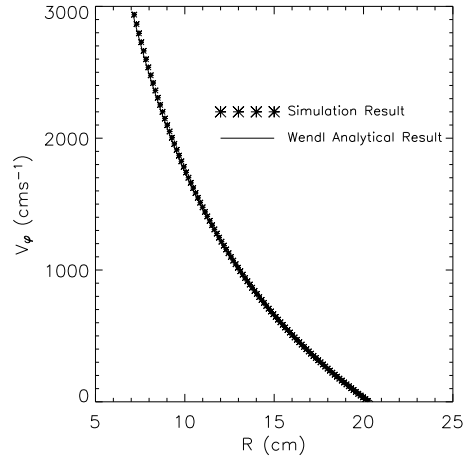


Fig. 3.— Comparison with incompressible code at $Re = 1600$: (a) Contours of toroidal velocity from Kageyama et al. (2004) (b) Results from ZEUS-2D with $M = 1/4$

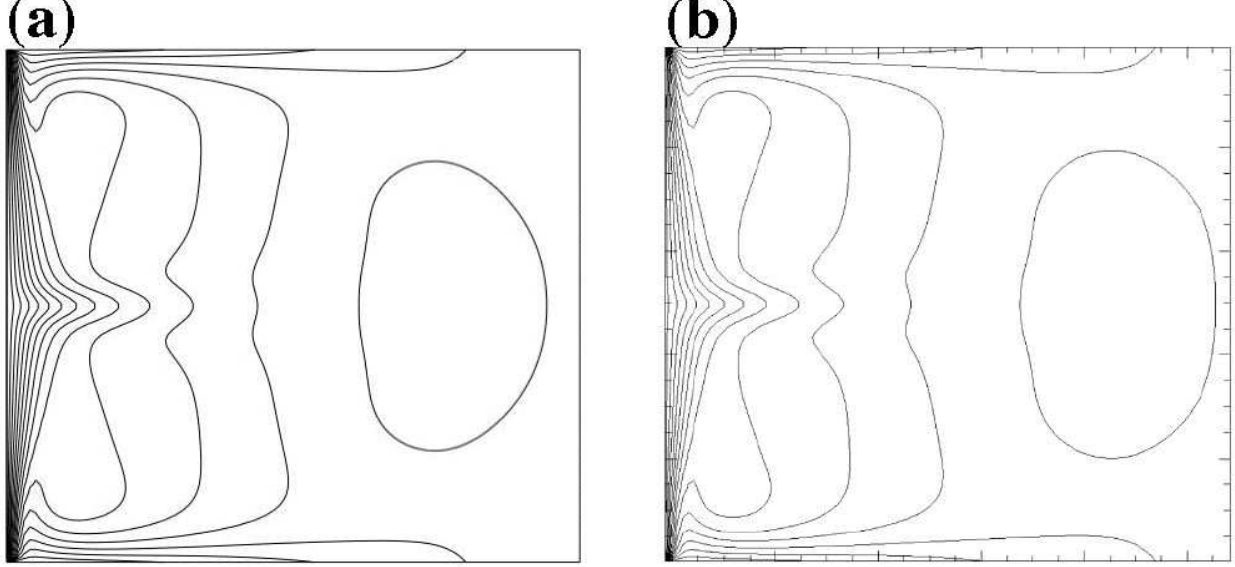


Fig. 4.— MRI growth rate versus Rm for conducting radial boundaries. *Points*: simulations. *Curve*: global linear analysis (Goodman & Ji 2002) with $Re = 25,600$.

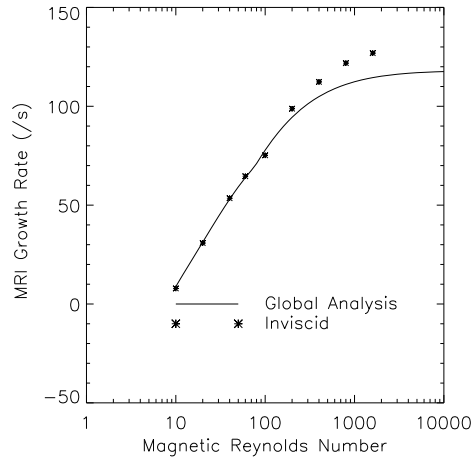


Fig. 5.— Angular velocity profile before and after saturation at several heights, for $Re = Rm = 400$. “Jet” is centered at $z = 0$ (squares).

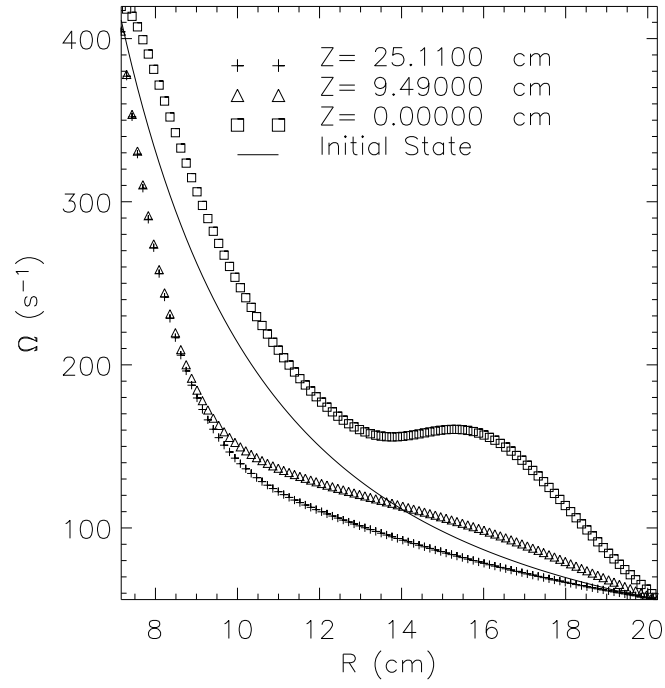


Fig. 6.— Contour plots of final-state velocities and fields. $Re = 400$, $Rm = 400$. (a) Poloidal flux function Ψ (Gauss cm²) (b) Poloidal stream function Φ (cm²s⁻¹) (c) toroidal field B_φ (Gauss) (d) angular velocity $\Omega \equiv r^{-1}V_\varphi$ (rad s⁻¹)

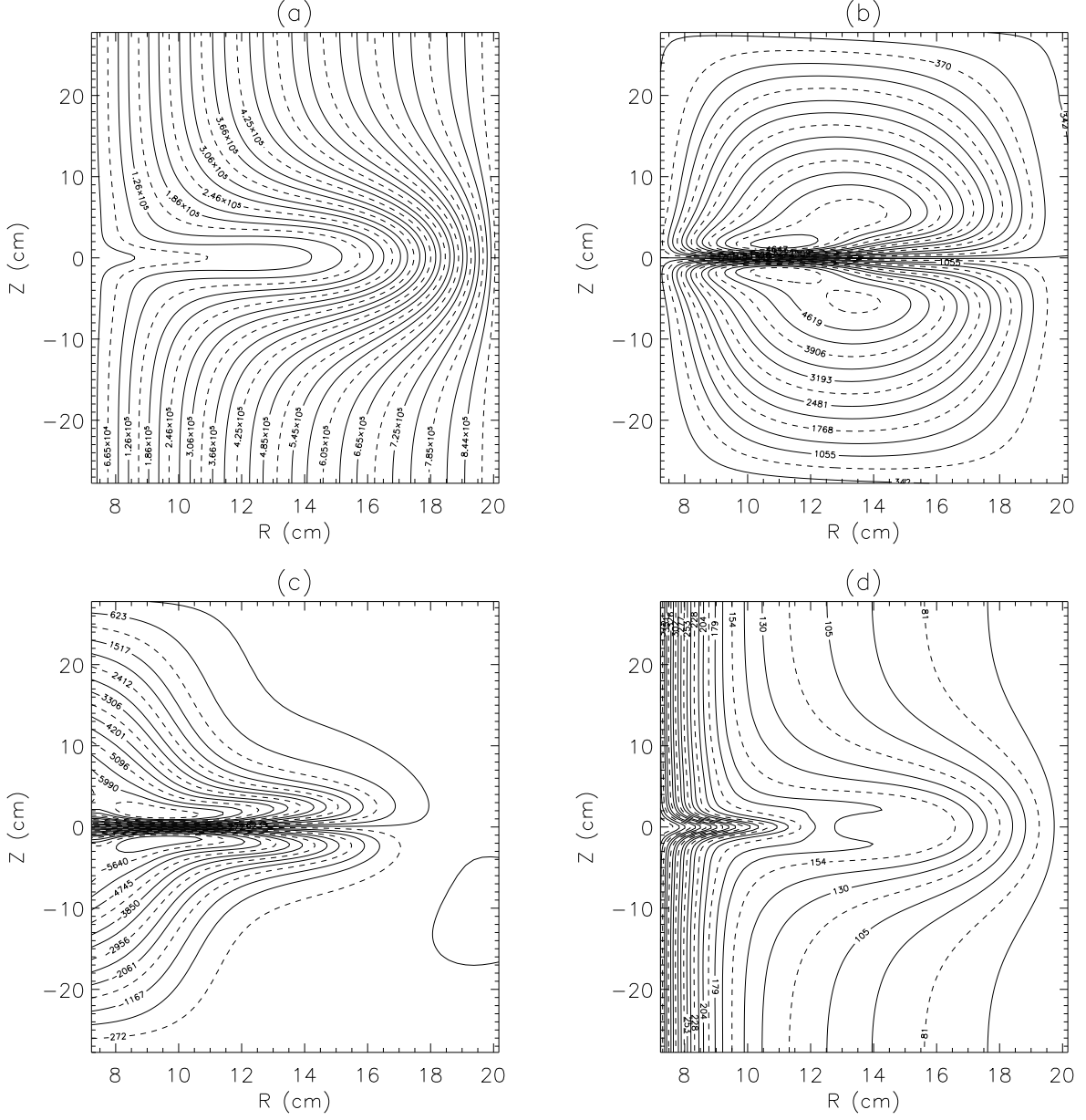


Fig. 7.— Radial velocity versus z for $Re = 400$, at several radii (cm): $+$, 8.42; $*$, 10.27; \times , 11.98; \triangle , 13.70; \diamond , 16.87; \square , 18.98. For clarity, only half the full vertical period (56 cm) is shown. Panel (a), $Rm = 400$; panel (b) $Rm = 6400$.

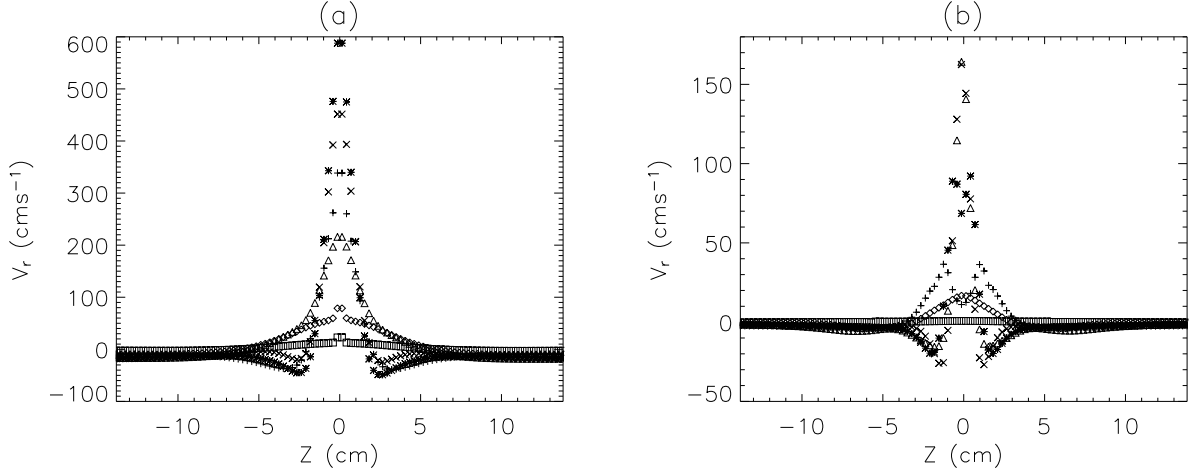


Fig. 8.— Maximum radial speed in the jet (left panel) and maximum of poloidal stream function (right panel) *vs.* magnetic Reynolds number, for $Re = 400$. Powerlaw fits are shown as dashed lines with slopes -0.53 [left panel, eq. (12)] and -0.57 [right panel].

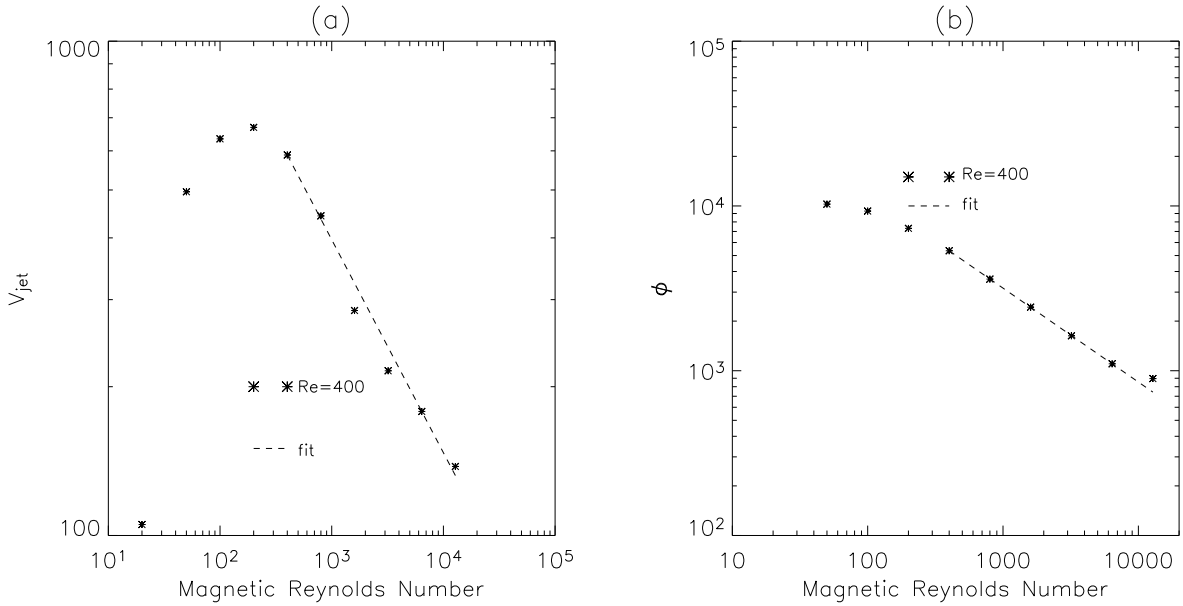


Fig. 9.— z -integrated torques versus r . $Re = 400$, $Rm = 400$. Left panel: initial state; right: final state

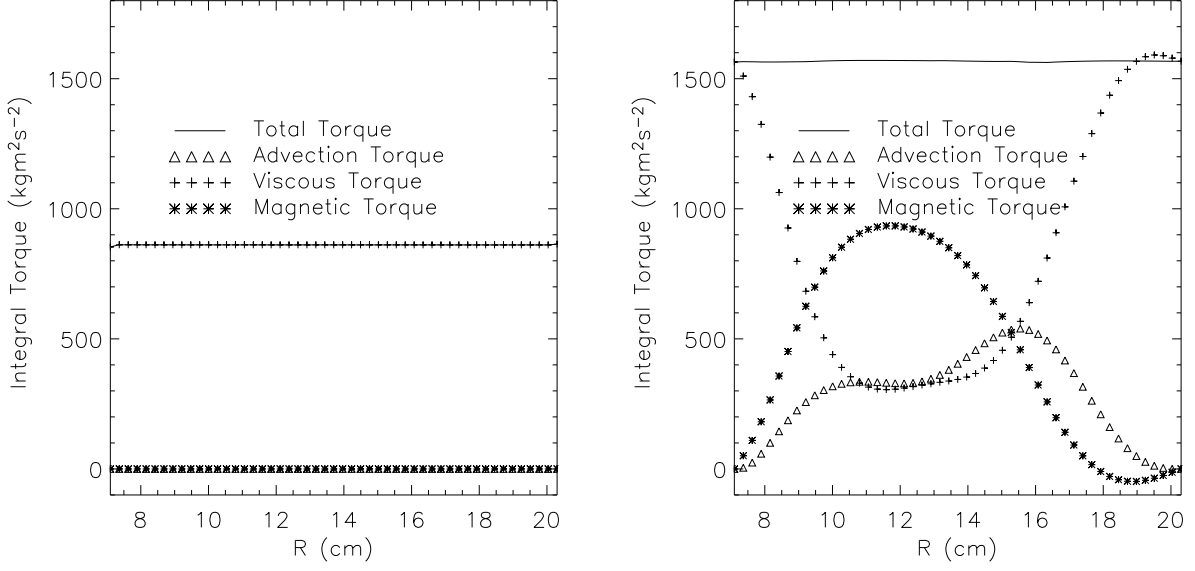


Fig. 10.— Increase of total torque versus (a) Rm and (b) Re . In panel (b), dashed lines have slopes of 0.5 ($Rm = 400$) and 0.675 ($Rm = 20$).

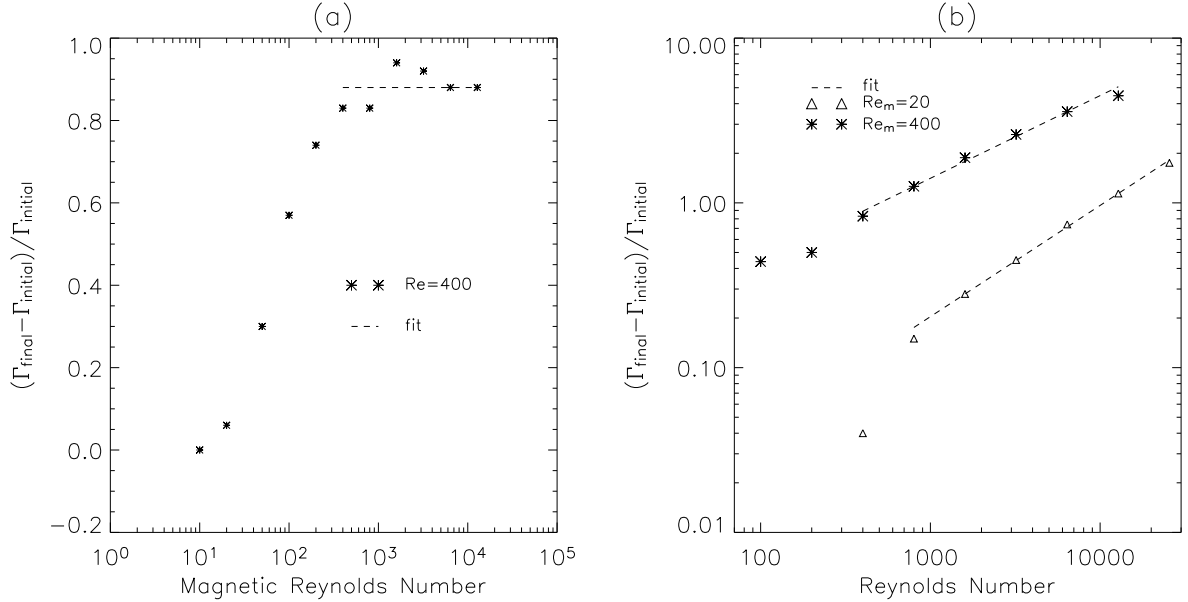


Fig. 11.— Total toroidal magnetic energy *vs.* time at $Re = 400$.

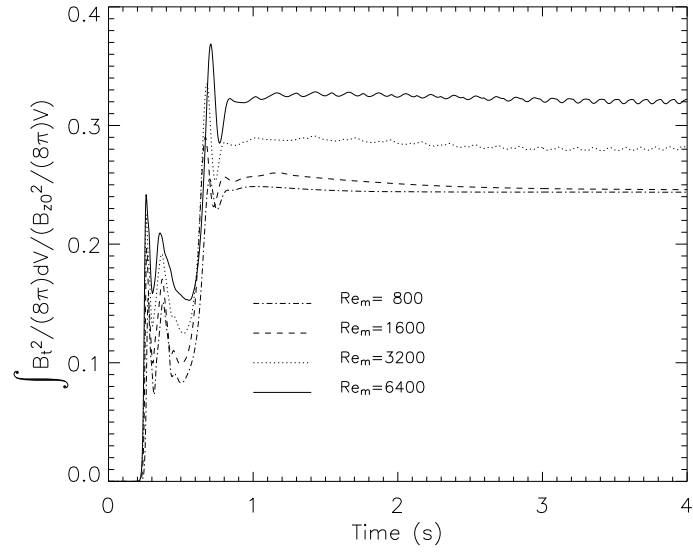


Fig. 12.— Like Fig. 6, but for $Rm = 6400$, $Re = 400$. Symmetry about $z = 0$ has not been enforced; the jet forms spontaneously at $z \approx -20$, but the whole pattern has been shifted vertically to ease comparison with Fig. 6.

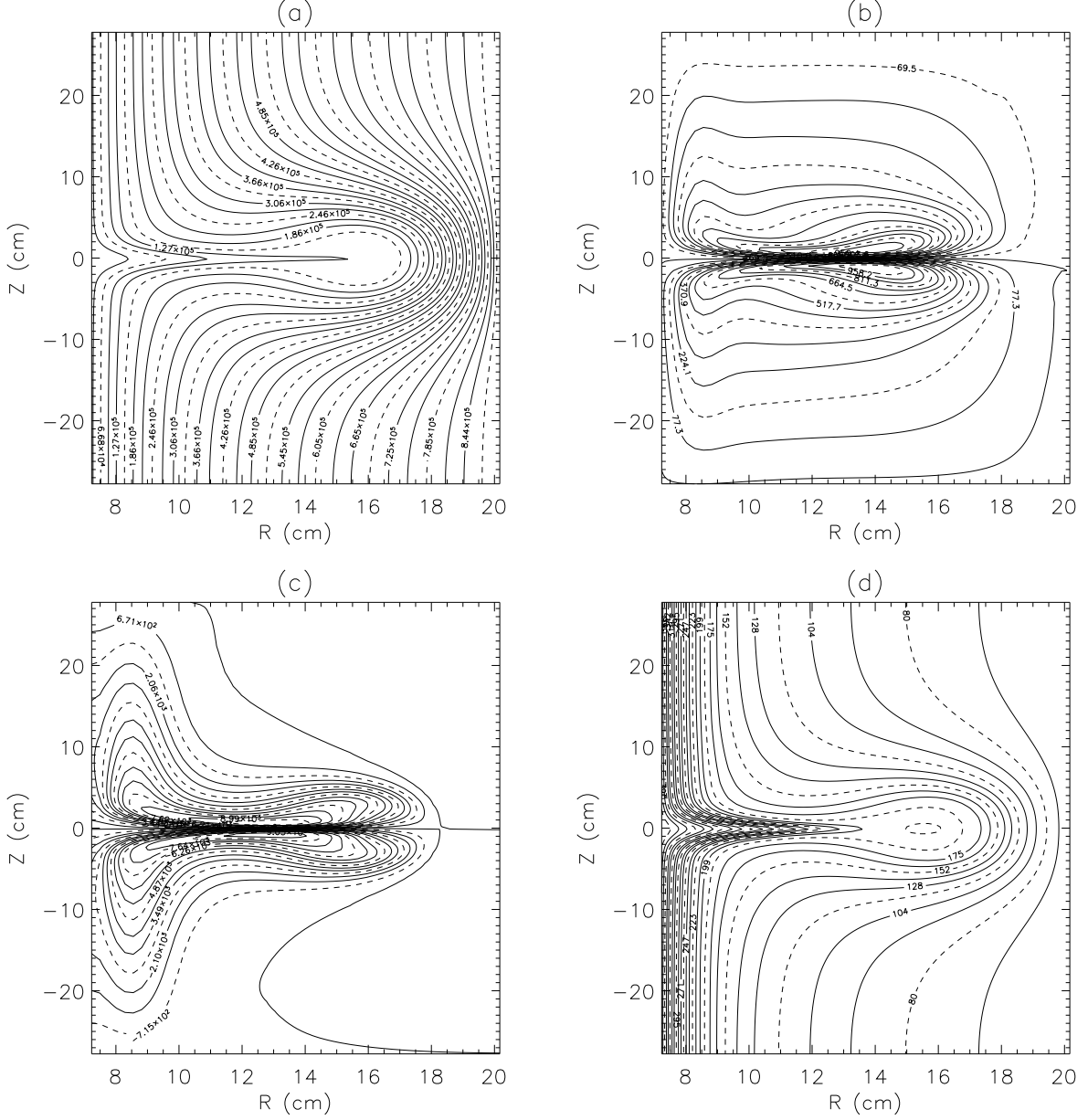


Fig. 13.— Maximum radial current in the current sheet (left panel) and maximum of toroidal magnetic field (right panel) *vs.* magnetic Reynolds number, for $Re = 400$. Powerlaw fits are shown as dashed lines with slopes 0.46 [left panel] and 0.18 [right panel, eq (22)].

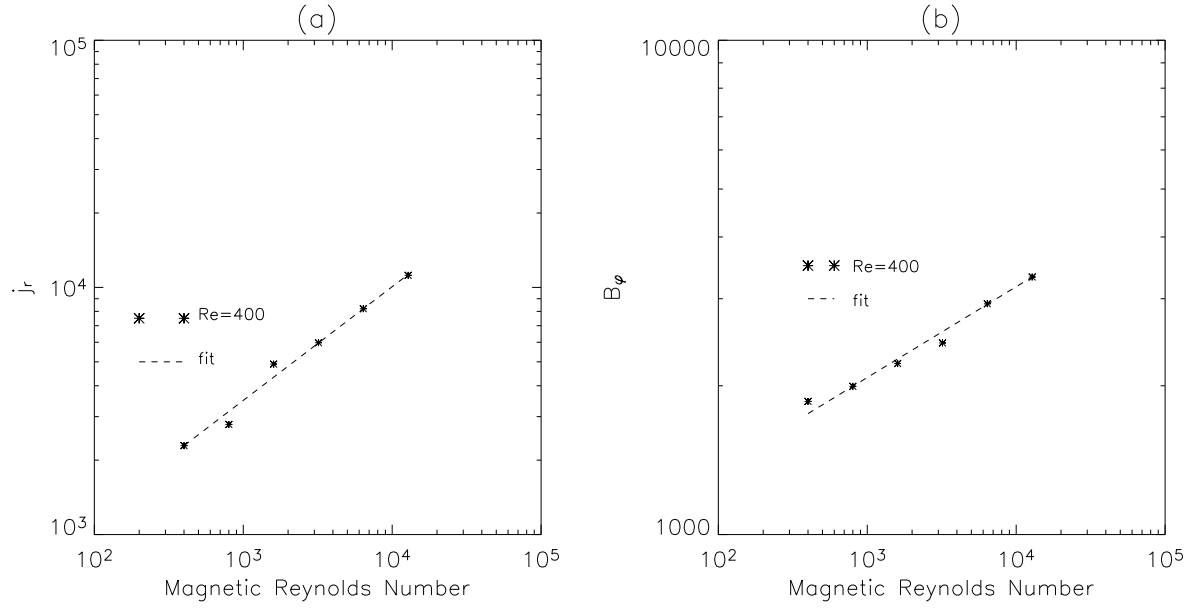


Fig. 14.— Like Fig. 6, but for $Re = 25600$, $Rm = 20$. The flow is unsteady but closely resembles steady flows at lower Re for this Rm .

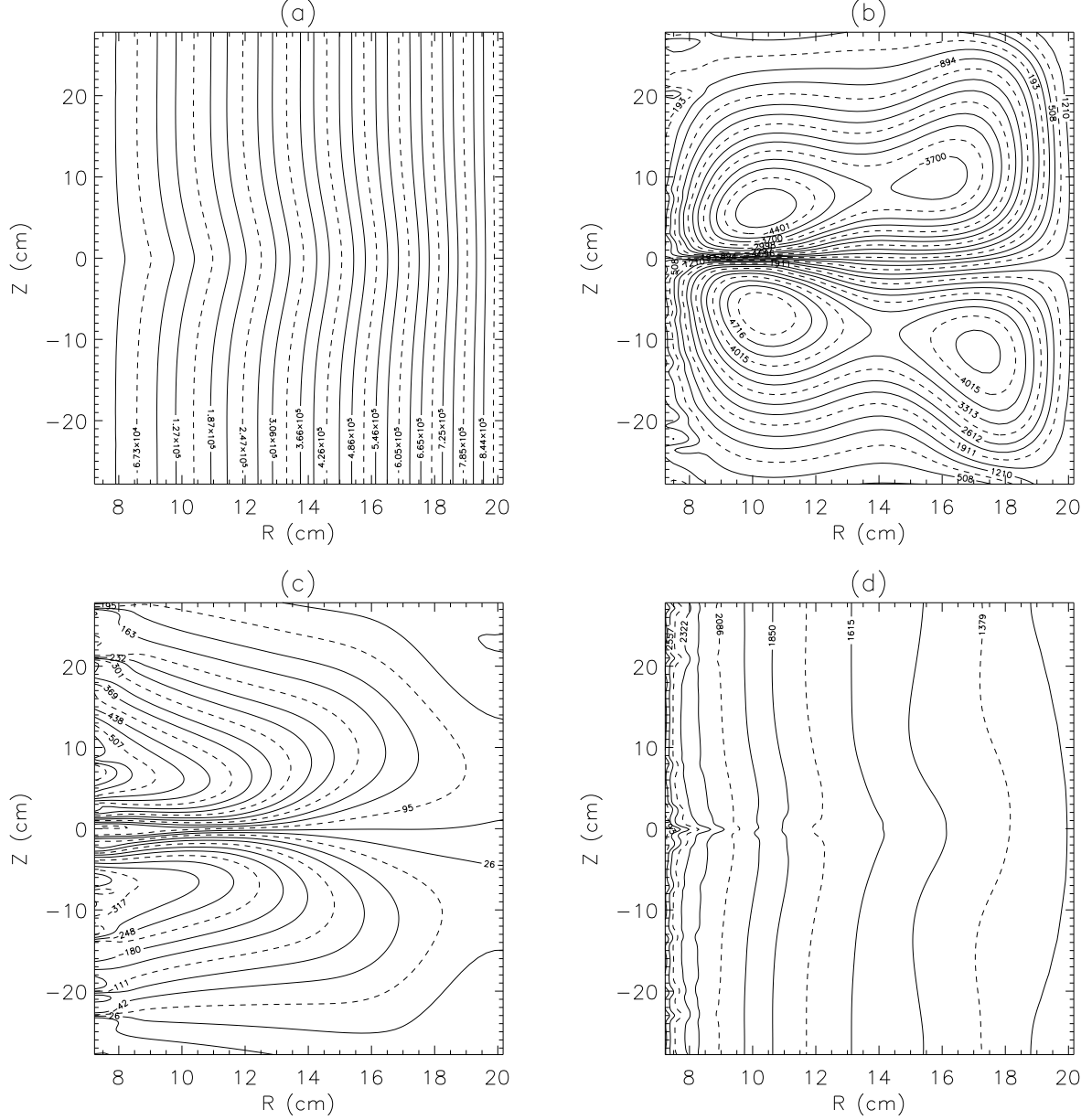


Fig. 15.— The z -averaged torques as in Fig. 9, but for the state shown in Fig. 14 ($Re = 25600$, $Rm = 20$). The radial variation of the total torque, though slight, testifies to the unsteadiness of the flow.

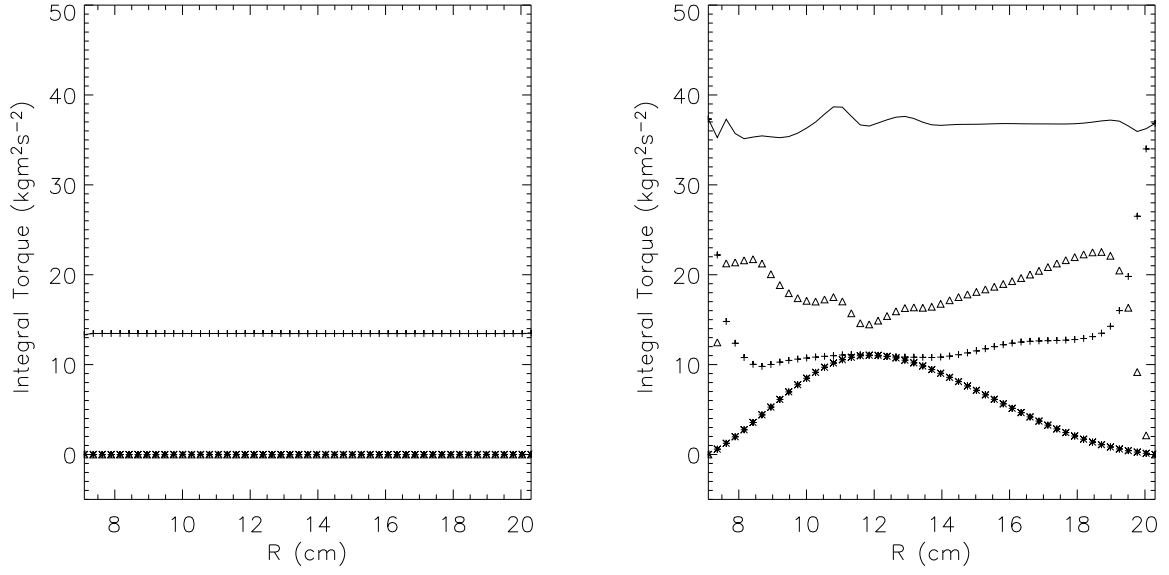


Table 1: Magnetic Diffusion Test

Rm	Resolution	Decay Rate [s^{-1}]	Exact Rate	Error (%)
400	100x100	382.52642	392.26048	2.482
400	50x50	352.76963	391.87454	9.979
100	100x100	1533.6460	1569.0419	2.256
100	50x50	1420.4078	1567.4982	9.384

Table 2: Growth rates from semianalytic linear analysis *vs.* simulation.

Rm	Re	n	Prediction [s^{-1}]	Simulation [s^{-1}]
400	400	1	41.67	77.66**
		2	72.71	
		3	77.69*	
		4	56.88	
		5	0.283	
20	∞	1	23.31	30.83**
		2	32.43*	
		3	23.73	
		4	6.905	

Table 3: Increase of total torque versus Re and Rm .

Rm	Re	Resolution $N_z \times N_r$	Γ_{initial} [kg m ² s ⁻²]	Γ_{final} [kg m ² s ⁻²]	$\Delta\Gamma/\Gamma_{\text{initial}}$
10	400	200×50	8.60e2	8.60e2	0.00
20	400	200×50	8.60e2	9.08e2	0.06
50	400	200×50	8.60e2	1.12e3	0.30
100	400	200×50	8.60e2	1.35e3	0.57
200	400	200×50	8.60e2	1.50e3	0.74
400	400	200×50	8.60e2	1.57e3	0.83
800	400	200×50	8.60e2	1.57e3	0.83
1600	400	200×50	8.60e2	1.67e3	0.94
3200	400	200×50	8.60e2	1.65e3	0.92
6400	400	200×50	8.60e2	1.62e3	0.88
12800	400	228×50	8.60e2	1.62e3	0.88
400	100	200×50	3.44e3	4.45e3	0.44
400	200	200×50	1.72e3	2.58e3	0.50
400	400	200×50	8.60e2	1.57e3	0.83
400	800	200×50	4.30e2	9.70e2	1.26
400	1600	200×50	2.15e2	6.20e2	1.88
400	3200	200×50	1.08e2	3.90e2	2.63
400	6400	200×50	5.38e1	2.46e2	3.58
400	12800	228×58	2.69e1	1.55e2	4.77
20	100	200×50	3.44e3	3.44e3	0.00
20	200	200×50	1.72e3	1.72e3	0.00
20	400	200×50	8.60e2	8.95e2	0.04
20	800	200×50	4.30e2	4.95e2	0.15
20	1600	200×50	2.15e2	2.76e2	0.28
20	3200	200×50	1.08e2	1.57e2	0.45
20	6400	200×50	5.38e1	9.35e1	0.74
20	12800	228×50	2.69e1	5.75e1	1.14
20	25600	320×50	1.34e1	3.70e1	1.75